Nano Research

Open Access

Research Article

Threefold programmable encoding for optical encryption by ferroelectric-assisted modulation of excitonic states in WSe_2

Weifeng Zhao[1,2,3,§], Yi Hong[1,2,§], Jiajun Zhong[1,2,§], Zihan Gao[1,2], Xinkai Zhu[1,2], Fangkai Wang[1,2], Weijiang Yi[1,2], Yufeng Shan[1,2], He Zhu[1,2], Feng Qiu[1,2], Zhiming Huang[1,2,3] ✉, Huizhen Wu[1,2,4], Ning Dai[1,2,3,5] ✉, and Jiaqi Zhu[1,2] ✉

[1] *Infrared material fellowship (IMF), Hangzhou Institute for Advanced Study, University of Chinese Academy of Sciences, Hangzhou 310024, China*
[2] *University of Chinese Academy of Sciences, Chinese Academy of Sciences, Beijing 100049, China*
[3] *State Key Laboratory of Infrared Physics, Shanghai Institute of Technical Physics, Chinese Academy of Sciences, Shanghai 200083, China*
[4] *School of Physics, Zhejiang University, Hangzhou 310027, China*
[5] *Jiangsu Collaborative Innovation Center of Photovoltaic Science and Engineering, Changzhou University, Changzhou 213164, China*
§ *Weifeng Zhao, Yi Hong, and Jiajun Zhong contributed equally to this work.*

Cite this article: *Nano Research*, **2026**, *19*, 94908718. https://doi.org/10.26599/NR.2026.94908718

ABSTRACT: In the era of rapid development of digital communication, the secure transmission of data is becoming increasingly important. This study proposes a novel optical encryption method utilizing multidimensional field control in a MoS_2/WSe_2 heterojunction integrated with a ferroelectric $Pb(Zr,Ti)O_3$ (PZT) layer. Benefiting from the spontaneous polarization of the PZT layer, free charges in the heterojunction are redistributed, making excitonic states in the WSe_2 highly adjustable. By dynamically controlling excitonic states through a multidimensional field involving laser power, lateral bias, and vertical bias, we achieve precise modulation of the energy levels and intensity ratio of neutral exciton and trion in WSe_2 via photoluminescence measurements. This multidimensional field-programmable method provides a new route for optical encoding and encrypted information transmission, overcoming the limitations of conventional single or dual field modulation systems. Our work highlights the potential of multidimensional field exciton modulation in energy-efficient and reconfigurable optical encryption systems, with broad applications in secure communication.

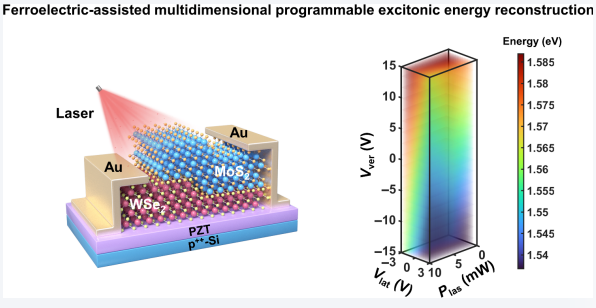

KEYWORDS: optical encryption, ferroelectric-assisted, multidimensional field control, exciton dynamics, reconfigurable optical devices

1 Introduction

In today's digital age, secure communication is the foundation for protecting privacy and ensuring the integrity of sensitive data. With the rapid growth of network data volume, the risk of network attacks also increases, and thus the demand for advanced encryption systems is becoming increasingly urgent. Optical encryption, which utilizes the unique properties of light, has been proven to be a promising method for secure data transmission [1, 2]. The adjustable character of excitonic states in two-dimensional (2D) transition metal dichalcogenides (TMDs) with high exciton binding energy provides a new paradigm for optical encryption [3–5]. Secure and efficient information encoding can be achieved by precisely modulating different excitonic states of TMDs [6], which provides strong security and high-speed data transmission and further makes this material system one of the most attractive solutions in future encryption systems.

Conventional optical encryption methods, such as phase modulation [6, 7] and amplitude modulation [8], rely on static optical properties [9], which limit their capability to adapt to the increasingly evolving encryption requirements [10]. Similarly, optical encryption methods based on TMDs typically employ single-dimensional control as well, such as a vertical gate electric field [3, 11–13], resulting in unidirectional or transient responses. When neutral exciton (X^0) and trion (X^t) coexist in TMDs, energy and composition cannot be independently modulated simultaneously, and this bottleneck problem severely restricts the development of

Received: December 17, 2025; **Revised:** March 17, 2026
Accepted: April 7, 2026

✉Address correspondence to Zhiming Huang, zmhuang@mail.sitp.ac.cn; Ning Dai, ndai@mail.sitp.ac.cn; Jiaqi Zhu, jiaqizhu@ucas.ac.cn

multidimensional controls [14–16]. Furthermore, these systems usually lack flexibility and real-time performance, making them more vulnerable to attacks [17]. Therefore, developing new methods to modulate excitonic states in multiple dimensions independently is highly desired for advanced optical encryption technology.

In this study, we introduce a multidimensional field control method for optical encryption, using a van der Waals (vdW) MoS_2/WSe_2 heterojunction integrated on a ferroelectric $Pb(Zr,Ti)O_3$ (PZT) layer. By combining three dimensions involving laser power (P_{las}), lateral bias (V_{lat}), and vertical bias (V_{ver}), we achieve dynamic and reversible modulation of excitonic states in the WSe_2, enabling precise control of excitonic energy. This multidimensional control overcomes the limitations of conventional methods, providing a flexible and more energy-efficient solution for optical encryption [18, 19]. The synergy between ferroelectric field modulation and exciton dynamics provides a powerful new scheme for secure optical communication and proposes a new concept for reconfigurable and low-power encryption systems in real time.

2 Results and discussion

2.1 Device architecture and baseline excitonic emission without external bias

We fabricate a MoS_2/WSe_2 vdW heterojunction on a ferroelectric PZT layer coated on a p^{++}-silicon (Si) substrate. Two gold (Au) electrodes are respectively applied to the WSe_2 and the MoS_2, defining an in-plane (lateral) channel for the application of V_{lat}. The out-of-plane (vertical) V_{ver} is applied through the p^{++}-Si, with the PZT acting as the ferroelectric dielectric (Fig. 1(a)). P_{las} serves both as an optical probe and a controllable input. "Baseline excitonic emission without external bias" refers to the situation where $V_{lat} = V_{ver} = 0$, with a fixed low P_{las}. The external applied electrical biases are set to zero and does not imply a strictly field-free condition: The heterojunction may still exhibit a built-in electric field, and the spontaneous polarization of the ferroelectric PZT substrate can induce an effective local field within the device. The PZT layer maintains a fixed polarization P before measurements. WSe_2 and MoS_2 flakes are transferred sequentially using a polydimethylsiloxane (PDMS)-assisted dry-transfer method. Importantly, after annealing, the X^0 in WSe_2 remains nearly unchanged, while the X^t exhibits a blueshift, indicating reduced carrier doping and suppressed charge trapping in the heterojunction (Fig. S1 in the Electronic Supplementary Material (ESM)). The successful construction of the heterojunction was verified by optical microscopy and Raman spectroscopy (Figs. 1(b) and 1(c)). The thicknesses of the WSe_2 and the MoS_2 are both ~ 4 nm, confirmed by an atomic force microscope (AFM), indicating that both materials consist of fewer than 10 atomic layers (Fig. S2 in the ESM).

Photoluminescence (PL) measurements under zero electrical fields establish the baseline excitonic emission without external bias (Figs. 1(d) and 1(e)). The WSe_2 region exhibits both X^0 and X^t. Gaussian fits show energy splitting (ΔE) of 92 meV for WSe_2 and 91 meV for the heterojunction. In monolayer WSe_2, ΔE is typically stable and small [20], which is generally attributed to the intrinsic trion binding energy. However, in our study, the ferroelectric PZT substrate amplified the ΔE and induced spectral broadening. The strong spontaneous polarization field and local electric field of PZT significantly altered the carrier concentration, local dielectric environment, and band bending in WSe_2, thereby modulating the excitonic states. The intensity ratio (I_{X^t}/I_{X^0}) increases from 1.99 for WSe_2 to 3.33 for the junction. To ensure reproducibility, PL mapping from another sample configuration (Fig. S3 in the ESM) confirms distinct PL contrast between the WSe_2 and MoS_2 regions. The similar ΔE but enhanced I_{X^t}/I_{X^0} at the junction indicates stronger carrier doping and charge transfer, even without external bias.

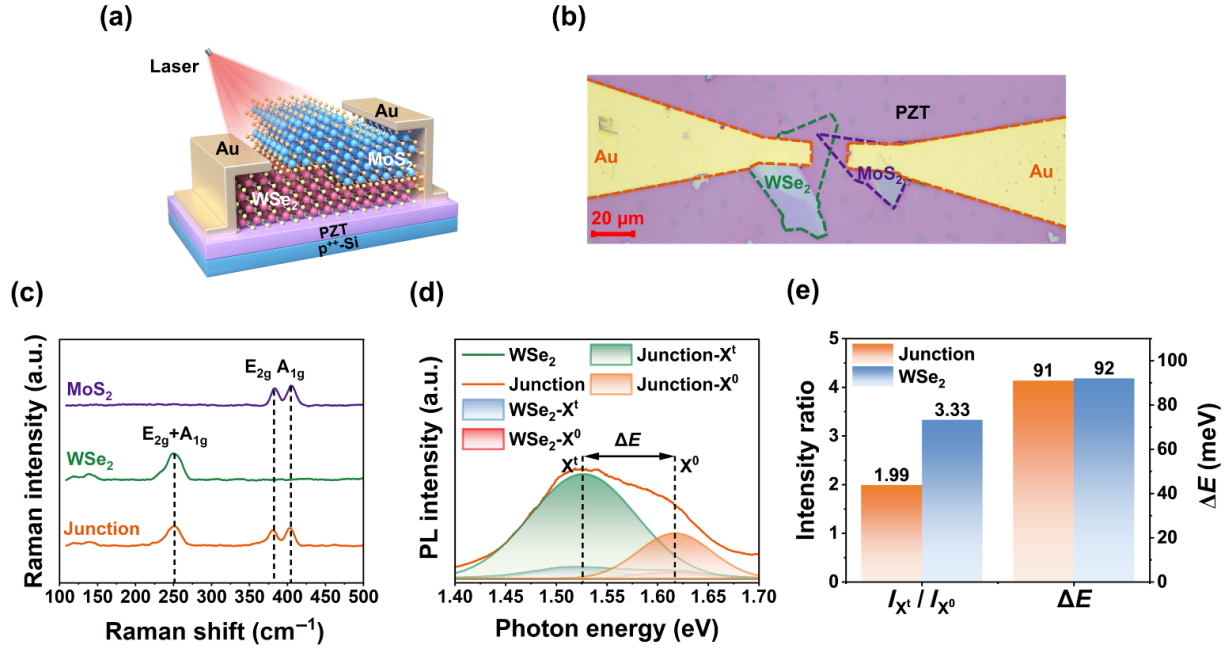

Figure 1 (a) Schematic of the MoS_2/WSe_2 heterojunction on a PZT layer with Au contacts. (b) Optical micrograph of a representative device. Dashed outlines highlight the WSe_2 (green) and MoS_2 (purple) regions. Scale bar: 20 μm. (c) Raman spectra of WSe_2, MoS_2, and the junction region. Peak positions remain almost unchanged in the junction, indicating negligible strain or structural perturbation. (d) PL spectra without external bias, showing the contributions from X^0 and X^t. The energy splitting (ΔE) is highlighted. (e) Comparison of the intensity ratio I_{X^t}/I_{X^0} and ΔE without external bias (from Gaussian fits).

We focus on the PL spectra of the WSe_2 region within the MoS_2/WSe_2 heterojunction, which allows for independent control of the carrier density and exciton fraction in WSe_2 using three input dimensions: P_{las}, V_{lat}, and V_{ver}. We chose MoS_2 as the material for the following reasons. Firstly, the PL spectrum of MoS_2 has a significant energy gap compared to that of WSe_2 [21]. Secondly, both MoS_2 and WSe_2 are TMDs, and they have excellent interface quality [22]. Lastly, MoS_2 is an n-type semiconductor, while WSe_2 is a p-type semiconductor. The p-n junction formed between them has good electrical modulation properties, making it easier to perform electrical modulation through external electric fields. The PZT-MoS_2/WSe_2 heterojunction offers selective, wide-range, and reversible control of WSe_2 excitonic states.

2.2 Ferroelectric-assisted P_{las} modulation of WSe_2 excitonic states

In this section, we explore how P_{las} modulates the excitonic states in WSe_2 with the assistance of the ferroelectric PZT layer. The modulation of the X^0-X^t states is studied without external electrical fields (i.e., V_{lat}, $V_{ver} = 0$) while varying P_{las} from 0.5 to 10 mW.

PL spectra of WSe_2 (Figs. 2(a) and 2(b)) show a redshift in both the X^0 and the X^t peaks, accompanied by a redshift in the PL center-of-mass (COM) (i.e., obtained by unimodal Gaussian fitting of the overall emission) as P_{las} increases. The magnitude of this COM redshift is more pronounced in the PZT configuration (Fig. 2(b)) compared with the non-ferroelectric SiO_2 configuration (Fig. 2(a)), where the small redshift is likely due to thermal effects on the electrical structure of the WSe_2. The extracted peak energies of X^0, COM and X^t (Figs. 2(c) and 2(d)) show that all slopes in the PZT configuration are 3–6 times larger than those in the SiO_2 configuration. Besides, the behaviors of I_{X^t}/I_{X^0} and ΔE as P_{las} varies (Figs. 2(e) and 2(f)) further confirm that the PZT layer can increase the modulation depth effectively. In the SiO_2 configuration, I_{X^t}/I_{X^0} and ΔE remain nearly constant when P_{las} increases, indicating minimal changes in excitonic state densities and transition processes. On the contrary, in the PZT configuration, both I_{X^t}/I_{X^0}

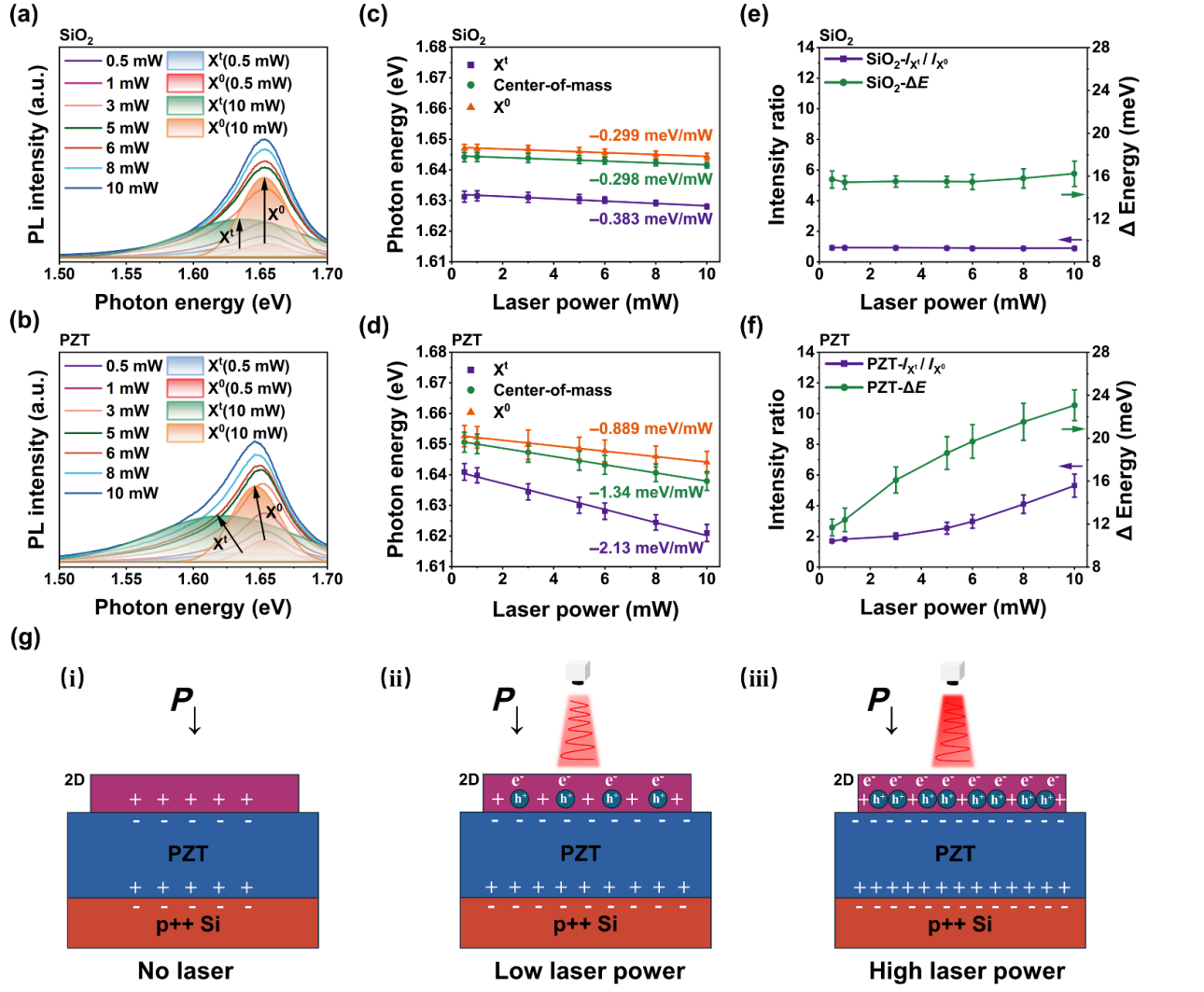

Figure 2 (a) and (b) PL spectra of WSe_2 on SiO_2 and PZT without external bias, as P_{las} increases from 0.5 to 10 mW. On SiO_2, the X^0 and X^t peaks show minimal shift; on PZT, both peaks redshift, with spectral weight shifting towards X^t. (c) and (d) Extracted peak energies of X^0 (orange), COM (green), and X^t (purple) as a function of P_{las}. The slopes in the PZT configuration are significantly larger, indicating enhanced modulation due to the ferroelectric PZT layer. (e) and (f) I_{X^t}/I_{X^0} (left) and ΔE (right) as a function of P_{las}. On SiO_2, both quantities remain nearly constant; on PZT, they increase with P_{las}, showing enhanced modulation. (g) Schematic illustrating the ferroelectric-assisted enhancement mechanism: With a fixed PZT polarization P, increasing P_{las} generates more photo-carriers in WSe_2, strengthening interfacial screening and photodoping. (i) No laser, (ii) Low laser power, (iii) High laser power.

and ΔE increase significantly with P_{las}, showing that the X^t proportion rises and the screening effect strengthens to modify the excitonic states. The above comparisons demonstrate the capability of the PZT layer to enhance the modulation depth of the excitonic states by varying P_{las}.

The mechanism of modulation enhancement is provided below. At room temperature, the spontaneous polarization of the PZT layer is directed downward (Fig. S4 in the ESM), therewith the top surface is negatively charged, and the bottom surface is positively charged (Fig. 2(g)). As P_{las} increases, more photo-generated carriers are produced in the photosensitive WSe_2. Subsequently, these holes are attracted by the negatively charged top surface of the PZT layer, increasing the free electron concentration in the WSe_2 region. This leads to bandgap renormalization (BGR) and a redshift in both the X^0 and X^t peaks (Fig. S5 in the ESM) [23–25]. Density functional theory (DFT) calculations under an out-of-plane electric field of 0–0.005 V/Å reveal a monotonic bandgap (E_g) narrowing in WSe_2, corroborating the BGR-driven redshift observed under ferroelectric-assisted laser excitation (Fig. S6 in the ESM). The redshift of X^t is more significant than that of X^0 due to its stronger coupling with the Fermi sea [26]. As the X^t proportion increases, both I_{X^t}/I_{X^0} and ΔE also increase. These results demonstrate the powerful role of ferroelectric enhancement in controlling the excitonic states in WSe_2 through P_{las} modulation, providing a route for precise and reversible control of excitonic properties in 2D materials.

2.3 Co-modulation by P_{las} and V_{lat}: Synergistic reconfiguration of WSe_2 excitonic states

In this section, we explore how the combined effects of P_{las} and V_{lat} modulate the excitonic states in WSe_2, focusing on their synergistic modulation. PL spectra were measured across a P_{las} range from 0.5 to 10 mW and a V_{lat} range from −3 to +3 V, with $V_{ver} = 0$.

At low power (0.5 mW, Fig. 3(a)) and high power (10 mW, Fig. 3(b)), the individual X^0 and X^t peak positions remain nearly unchanged as V_{lat} varies. However, the COM systematically shifts to lower energy, indicating spectral-weight reweighting rather than a direct shift of each peak. Linear fits (Figs. 3(c) and 3(d)) quantify this trend and confirm that higher P_{las} augments the COM redshift primarily through composition changes. The 2D map of COM energy (Fig. 3(e)) reveals a monotonic redshift with increasing P_{las} or more positive V_{lat}, while I_{X^t}/I_{X^0} (Fig. 3(f)) increases with more positive V_{lat} across the entire power range, suggesting enhanced modulation of excitonic states due to the combined effects of P_{las} and V_{lat}. The X^0, X^t energy maps, along with ΔE, are shown in Fig. S7 in the ESM for details.

The mechanism of this modulation is as follows. When V_{lat} is applied, it causes a spatial redistribution of net charges to alter the effective depletion region in the heterojunction [27, 28]. A positive V_{lat} shrinks the effective depletion region, yielding local accumulation of mobile carriers within the laser spot, while a negative V_{lat} tends to enlarge the effective depletion region, reducing the mobile carrier concentration here. The X^t proportion increases with the local free-electron density and raising I_{X^t}/I_{X^0}. Since X^t have lower energy, this results in a shifting of the COM to lower energy. P_{las} acts synergistically by raising the carrier density, further amplifying the reweighting induced by V_{lat}.

2.4 Antagonistic co-modulation by P_{las} and V_{ver}: Competing shifts of WSe_2 excitonic states

In this section, we explore the competing effects of P_{las} and V_{ver} on the excitonic states in WSe_2, focusing on the antagonistic co-modulation of exciton energies. PL spectra were measured across a P_{las} range from 0.5 to 10 mW and a V_{ver} range from −15 to + 15 V, with $V_{lat} = 0$.

At low power (0.5 mW, Fig. 4(a)), increasing V_{ver} causes both X^0 and X^t peaks to blueshift. At high power (10 mW, Fig. 4(b)), the exciton energy redshifts, but the X^t peak still blueshifts, while the X^0 peak redshifts. The different peak shifts indicate that the interplay

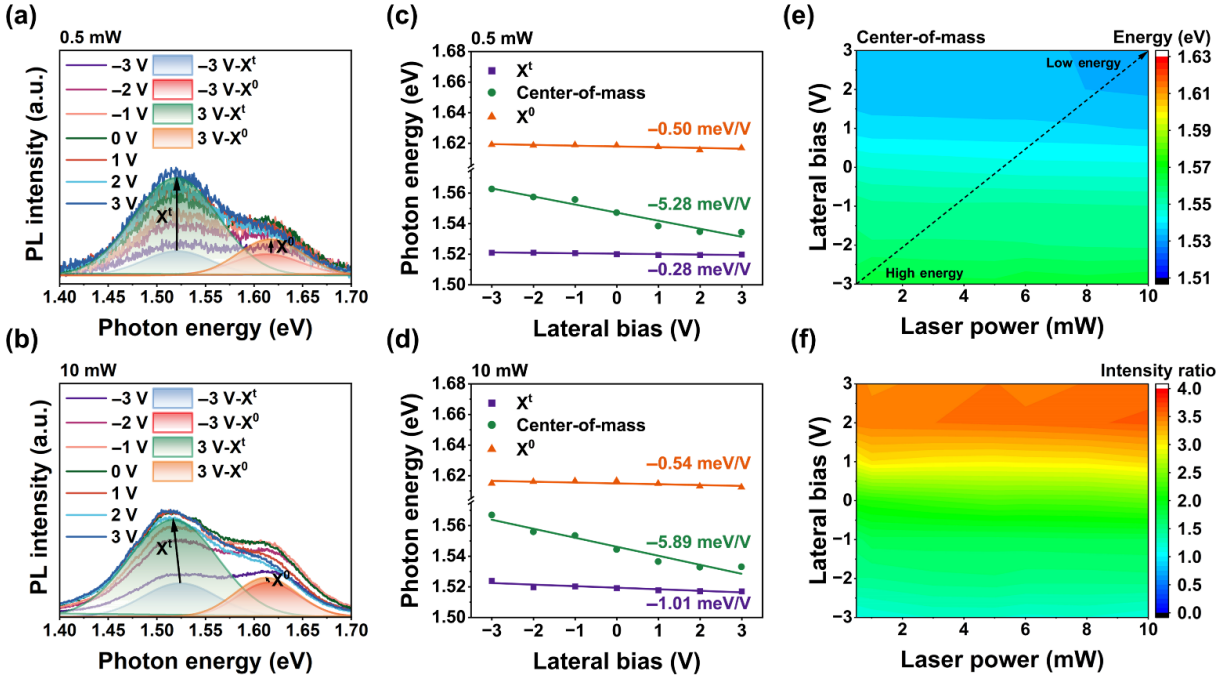

Figure 3 (a) and (b) PL spectra at 0.5 and 10 mW for V_{lat} in the range from −3 to +3 V. At 0.5 mW, the X^0 and X^t peaks remain nearly unchanged; at 10 mW, both peaks show redshift. (c) and (d) Extracted peak energies of X^0 (orange), COM (green), and X^t (purple) as a function of V_{lat}. The slopes are more pronounced, especially for X^t. (e) 2D map of COM energy as a function of V_{lat} and P_{las}. (f) I_{X^t}/I_{X^0} across the [P_{las}, V_{lat}] space, showing spectral-weight transfer toward X^t.

between P_{las} and V_{ver} creates competing shifts in the exciton peaks. Notably, at V_{ver} = −5 V, the intensity of both exciton peaks reaches its maximum, showing the most significant signal. For consistency, −15 and +15 V are chosen as the initial and final states to investigate the extreme polarization effects at both negative and positive V_{ver}.

Linear fits (Figs. 4(c) and 4(d)) quantify the trends. The negative slope for X^0 in Fig. 4(d) indicates that the blueshift of X^0 weakens at higher P_{las}, suggesting that carrier density and redistribution effects become more significant at 10 mW. The 2D COM map (Fig. 4(e)) highlights this competition: Energy increases with V_{ver} but decreases with P_{las}, producing a diagonal contour separating blue-shifted and red-shifted regimes. In parallel, I_{X^t}/I_{X^0} (Fig. 4(f)) decreases with more positive V_{ver} and increases with P_{las}. Detailed energy maps of X^0, X^t, and ΔE are shown in Fig. S8 in the ESM.

V_{ver} modulates the direction of the electric field in WSe_2 by altering the polarization direction of the PZT, which influences the distribution of carriers and thereby controls the charge state of the X^t. When $V_{ver} < 0$, the polarization of the PZT layer is directed downward (Figs. S4 and S9 in the ESM), attracting holes to the WSe_2 region, enhancing the formation of X^- (negative trion). This leads to a redshift of the exciton peaks due to the stronger binding energy of X^- (Fig. S10 in the ESM) [29, 30]. The blueshift of X^0 is due to a similar carrier redistribution effect, with the applied V_{ver} influencing the electron-hole interaction and making X^0 more spatially confined at lower carrier densities [14, 31]. In contrast, when $V_{ver} > 0$, the polarization is reversed, making the PZT surface positively charged, repelling electrons and attracting holes, favoring the formation of X^+ (positive trion). Since X^+ has weaker binding energy, it causes a blueshift in the PL spectrum.

2.5 Multidimensional field-programmable optical encryption and communication

We use three controls (P_{las}, V_{lat}, V_{ver}) to map the WSe_2 excitonic energy into programmable multidimensional domains. Figure 5(a) displays the resulting energy landscape reconstructed from discrete PL COM measurements at sampled [P_{las}, V_{lat}, V_{ver}] nodes, rendered on a regular grid using linear scattered-data interpolation (Table S1 in the ESM). These sampled conditions are used only for calibration of the multidimensional excitonic energy landscape and logic windows, rather than being required for every practical encoding/decoding operation. By adjusting the multidimensional control parameters of P_{las}, V_{lat}, and V_{ver}, we can modulate the energy levels and proportions of X^t and X^0 in multidimensional space, further controlling the energy distribution of the COM. This multidimensional field modulation technique not only allows for effective tuning of the excitonic energy distribution but also provides additional degrees of freedom for encoding, thereby enhancing the potential applications of optical encryption technology. By steering along redshift-dominant or blueshift-dominant directions (Fig. 5(b)), the exciton energy is quantized into preset windows using two thresholds E_{th1} and E_{th2} (Fig. 5(c)), forming a ternary alphabet: Logic1 ($E \leq E_{th2}$), Logic-1 ($E_{th2} < E < E_{th1}$) and Logic0 ($E \geq E_{th1}$). The setting of the two thresholds can be adjusted according to the user demand, thereby expanding the flexibility of the system and its potential applications.

Using this multidimensional field control, we generate the Info source (Fig. 5(d)). For each pixel, the triplet [P_{las}, V_{lat}, V_{ver}] is tuned so that the COM energy falls into a designated energy bin (Logic1/Logic-1/Logic0). During encryption, a user-defined Key (a pixel-wise matrix) determines how the target bins are permuted and masked across the array; the device applies the corresponding fields and outputs the encoded signal. At the receiver, decryption uses a password (PW) that implements the same permutation and mask as the Key. Only when PW = Key is the original pattern recovered, while any mismatch produces a scrambled output (Fig. S11 in the ESM). Users can periodically change the PW according to their needs, thereby enhancing the reliability of the

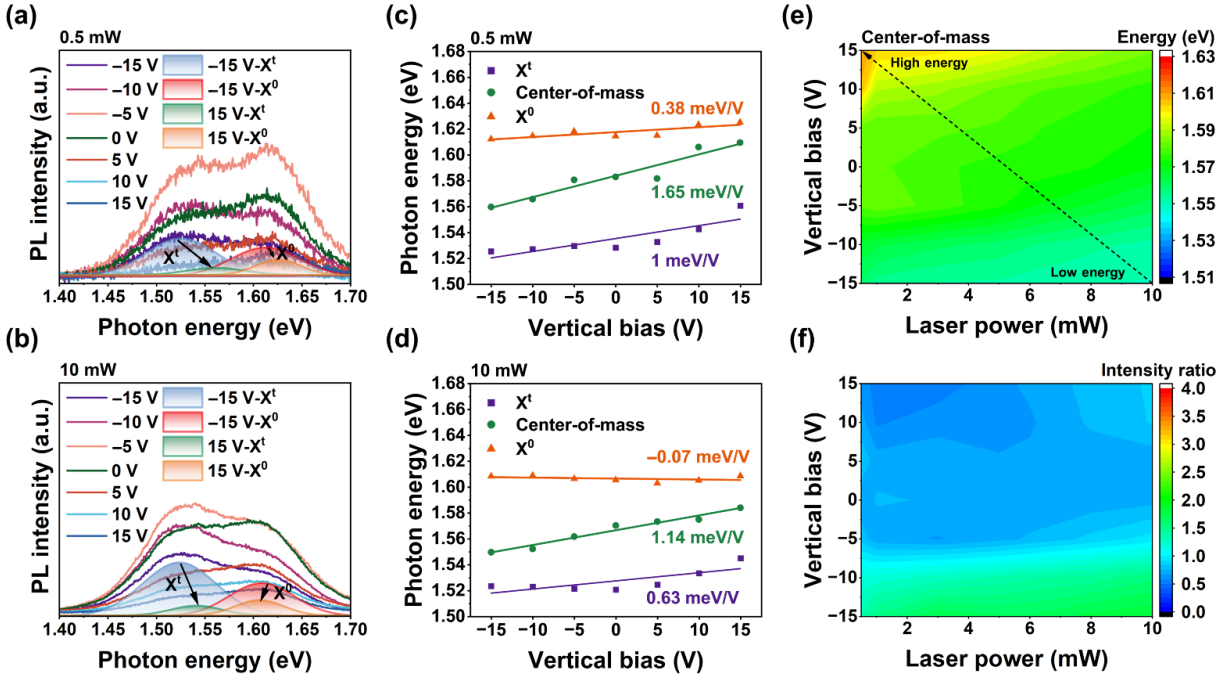

Figure 4 (a) and (b) PL spectra at 0.5 and 10 mW for V_{ver} in the range from −15 to +15 V. At 0.5 mW, both X^0 and X^t show a blueshift with increasing V_{ver}; at 10 mW, X^t shows a blueshift while X^0 undergoes a redshift. (c) and (d) Extracted peak energies of X^0 (orange), COM (green), and X^t (purple) as a function of V_{ver}. (e) 2D map of COM energy as a function of V_{ver} and P_{las}. (f) I_{X^t}/I_{X^0} across the [P_{las}, V_{ver}] space, showing a weak variation and a decreasing trend for more positive V_{ver}.

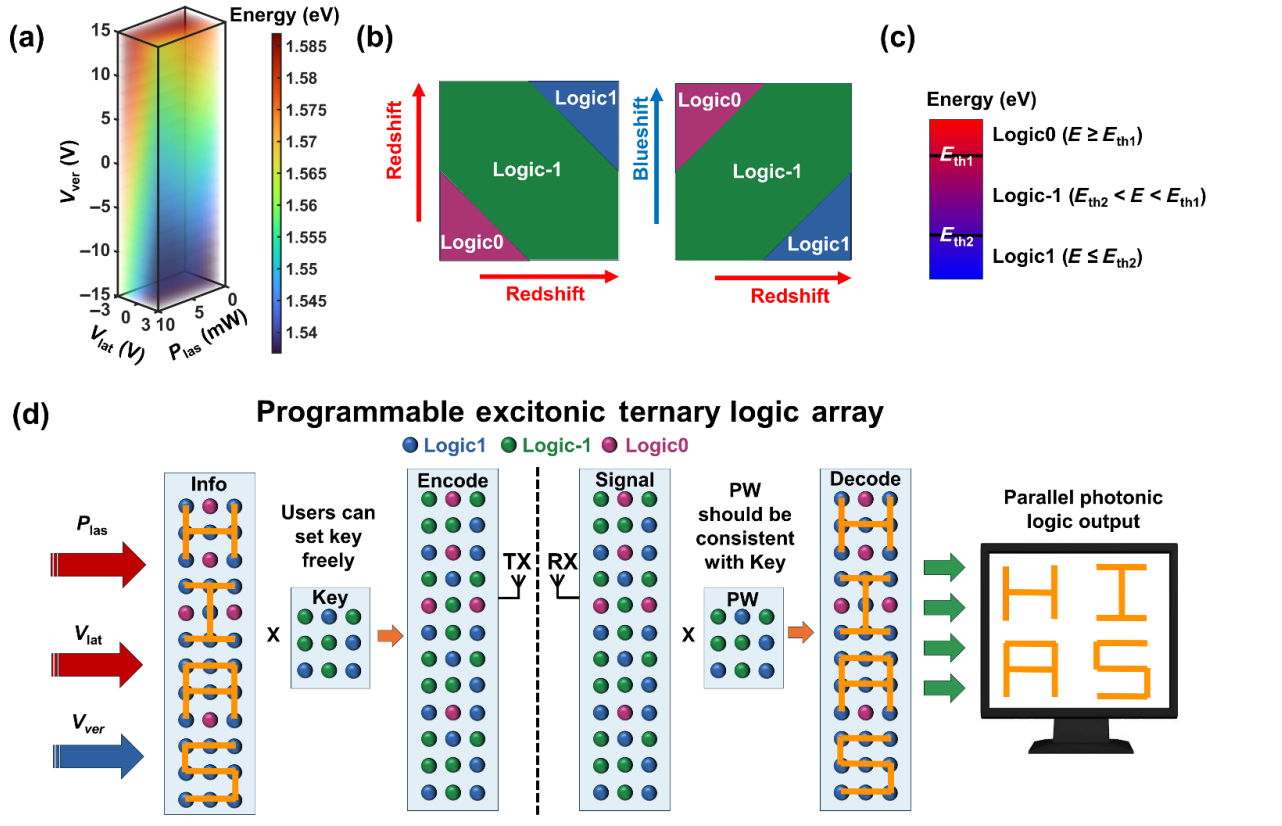

Figure 5 (a) Multidimensional landscape of the WSe_2 COM energy as a function of P_{las}, V_{lat}, V_{ver} on PZT, defining a three-input control space. (b) State maps showing how redshift-dominant (P_{las}/V_{lat}) and V_{ver}-induced blueshift regimes populate distinct regions in the energy plane. (c) Ternary quantization scheme for coding: two thresholds E_{th1}, E_{th2} map the measured energy to Logic0 ($E \geq E_{th1}$), Logic-1 ($E_{th2} < E < E_{th1}$), and Logic1 ($E \leq E_{th2}$). (d) Proof-of-concept programmable excitonic ternary logic array. A message ("Info") is encoded pixel-wise by applying a vector [P_{las}, V_{lat}, V_{ver}] together with a user-defined Key; at the receiver (RX), successful decode requires a matching password (i.e., PW = Key). The array yields parallel photonic logic outputs, demonstrated by reconstructing the pattern "HIAS".

system (Fig. S12 in the ESM). This multidimensional field programmability transforms the WSe_2 region into a reconfigurable optical encryption and communication platform: Keys are set and updated electronically or optically, pixel-parallel logic is achieved without hardware changes, and readout is performed by PL mapping and computer decoding for real-time operation. At the current stage, this work should be regarded as a proof-of-concept demonstration of multidimensional excitonic energy encoding, rather than a fully integrated or engineering-optimized platform. To compare the control dimensions and methods applied to excitonic states across different material systems, we summarize the relevant approaches in Table S2 in the ESM. From the comparison we can learn that only our method can achieve multidimensional controlling, which may boost the development of advanced optical encryption, computing, and communication technologies.

3 Experimental methods

3.1 Device fabrication

WSe_2 and MoS_2 flakes were mechanically exfoliated from bulk crystals using adhesive tape and transferred onto a PDMS film. Thin flakes with suitable thickness and size were confirmed under an optical microscope and then sequentially stacked onto a p^{++}-Si substrate coated with a PZT ferroelectric layer by a dry-transfer method. After each transfer, the samples were cleaned in acetone, ethanol, and deionized water to remove polymer residues, followed by annealing at 150 °C for 2 h under nitrogen atmosphere to improve interlayer coupling and reduce interfacial contamination. After completing the stacking of the MoS_2/WSe_2 heterojunction, electrode regions were defined by laser lithography, and Au electrodes (~ 50 nm) were deposited by thermal evaporation to form electrical contacts.

3.2 Material characterizations

Raman and PL spectra were acquired using a confocal Raman/PL spectrometer (alpha300, WITec) with a 532 nm excitation laser. The laser beam was focused onto the sample surface through a 50× objective lens, resulting in a spot size of approximately 1 μm. The excitation power was controlled between 0.5 and 10 mW to prevent sample damage. The thickness of the two-dimensional materials and the polarization direction of PZT were characterized by atomic force microscopy and piezoresponse force microscopy (Dimension ICON, Bruker). For V_{lat} modulation, a source meter was employed to apply V_{lat} between the Au contacts on WSe_2 and MoS_2, from −3 to +3 V with 1 V steps. For V_{ver} modulation, the p^{++}-Si served as the back-gate electrode, and V_{ver} was stepped from −15 to +15 V with 5 V steps. "Without external bias" corresponded to $V_{lat} = V_{ver} = 0$. P_{las} served both as an optical probe and as one of the three control inputs. All optical and electrical measurements were performed at room temperature.

3.3 Spectral data analysis

The PL spectra were analyzed using multi-peak Gaussian fitting to separate the contributions of X^0 and X^t. Reasonable constraints on

peak positions and full width at half maximum (FWHM) were applied during the fitting process to ensure reliable separation of overlapping components. To verify the robustness of the peak separation, PL spectra collected from three different positions were analyzed using the same fitting window, baseline treatment, initial parameter range, and peak-shape constraints. The extracted peak positions showed good statistical stability under these unified fitting conditions, supporting the reliability of the X^t/X^0 deconvolution. The COM was obtained by unimodal Gaussian fitting of the overall emission. The ΔE was extracted from the fitted peak positions, while the I_{X^t}/I_{X^0} was calculated by integrating the corresponding Gaussian peak areas. All spectral fittings and numerical analyses were performed using OriginPro and Python scripts.

4 Conclusions

In this study, we present a novel multidimensional field-programmable scheme for reconfiguring WSe_2 excitonic states on a ferroelectric PZT layer at room temperature. The system employs three orthogonal fields (P_{las}, V_{lat}, and V_{ver}) to provide precise and reversible control of excitonic states. We observe that increasing P_{las} induces a ferroelectric-assisted redshift of both X^0 and X^t, and an increase in the intensity ratio of X^t to X^0. V_{lat} redistributes the exciton intensity ratio, resulting in a significant redshift of the COM. In contrast, V_{ver} antagonizes P_{las} effects by inducing a blueshift for both X^0 and X^t at low P_{las}, while at higher P_{las}, X^t blueshifts and X^0 redshifts. Furthermore, we demonstrate how the interactions among these fields enable programmable excitonic ternary logic, which can be used for optical encryption and communication. The system's reconfigurability and energy-efficient operation make it a promising platform for excitonic optoelectronic applications. This work highlights the potential of ferroelectric field modulation, combined with multidimensional control of excitonic states, as a path toward flexible and energy-efficient optical computing architectures.

Electronic Supplementary Material: Supplementary material (Figs. S1–S12 and Tables S1 and S2) is available in the online version of this article at https://doi.org/10.26599/NR.2026.94908718.

Data availability

All data needed to support the conclusions in the paper are presented in the manuscript and the Electronic Supplementary Material. Additional data related to this paper may be requested from the corresponding author upon request.

Acknowledgements

This work is granted by the National Natural Science Foundation of China (No. 62504059), Zhejiang Provincial Natural Science Foundation of China (No. LD25F040001), Hangzhou Joint Fund of the Zhejiang Provincial Natural Science Foundation of China (No. LHZON25F050001), the National Key Research and Development Program of China (No. 2023YFA1608701), Hangzhou Natural Science Foundation of China (No. 2025SZRJJ2051), and Hangzhou Key Scientific Research Project (No. 2024SZD1A39).

Declaration of competing interest

All the contributing authors report no conflict of interests in this work.

Author contribution statement

Z. M. H., N. D., and J. Q. Z. conceived this project. W. F. Z., Y. H., and J. J. Z. fabricated the devices. W. F. Z., Z. H. G., X. K. Z., F. K. W., and W. J. Y. conducted PL measurements and analysis. W. F. Z., Y. H., J. J. Z. performed data processing. Y. F. S., H. Z., F. Q., Z. M. H., H. Z. W., N. D., and J. Q. Z. advised on the experiments. W. F. Z. wrote the manuscript based on inputs from all the other authors. All authors have given approval to the final version of the manuscript.

Use of AI statement

None.

References

[1] Bian, L. H.; Chang, X. Y.; Jiang, S. W.; Yang, L. M.; Zhan, X. R.; Liu, S. C.; Li, D. Y.; Yan, R.; Gao, Z.; Zhang, J. Large-scale scattering-augmented optical encryption. *Nat. Commun.* **2024**, *15*, 9807.

[2] Ouyang, M.; Yu, H. Y.; Pan, D. P.; Wan, L.; Zhang, C.; Gao, S. C.; Feng, T. H.; Li, Z. H. Optical encryption in spatial frequencies of light fields with metasurfaces. *Optica* **2022**, *9*, 1022–1028.

[3] Wang, H.; Zhang, Z.; Huang, W. T.; Chen, P. H.; He, Y. P.; Ming, Z. Y.; Wang, Y.; Cheng, Z. G.; Shen, J. B.; Zhang, Z. X. Programmable optical encryption based on electrical-field-controlled exciton-trion transitions in monolayer WS_2. *ACS Appl. Mater. Interfaces* **2024**, *16*, 41099–41106.

[4] Chen, X. T.; Lian, Z.; Meng, Y. Z.; Ma, L.; Shi, S. F. Excitonic complexes in two-dimensional transition metal dichalcogenides. *Nat. Commun.* **2023**, *14*, 8233.

[5] Huang, G. Y.; Lin, L. H.; Zhao, S.; Li, W. B.; Deng, X. N.; Zhang, S. M.; Wang, C.; Li, X. Z.; Zhang, Y.; Fang, H. H. et al. All-optical reconfigurable excitonic charge states in monolayer MoS_2. *Nano Lett.* **2023**, *23*, 1514–1521.

[6] Wang, W. Q.; Wang, X. G.; Xu, B. J.; Chen, J. L. Optical image encryption and authentication using phase-only computer-generated hologram. *Opt. Lasers Eng.* **2021**, *146*, 106722.

[7] Zhang, L.; Lin, S. S.; Zhou, Q. M.; Xue, J. D.; Xu, B. J.; Wang, X. G. Speckle-based optical encryption with complex-amplitude coding and deep learning. *Opt. Express* **2023**, *31*, 35293–35304.

[8] Tang, J.; Li, Z.; Wan, S.; Wang, Z. J.; Wan, C. W.; Dai, C. J.; Li, Z. Y. Angular multiplexing nanoprinting with independent amplitude encryption based on visible-frequency metasurfaces. *ACS Appl. Mater. Interfaces* **2021**, *13*, 38623–38628.

[9] Yun, C.; Nam, S.; Kim, H.; Jung, W.; Choi, S. S. Advanced optical encryption using tunable color and polarization separation in *in-situ* polymerized chiral liquid crystals. *ACS Appl. Mater. Interfaces* **2025**, *17*, 12532–12543.

[10] Ji, Y.; Wen, X.; Zhou, X. Y.; Li, Y. T.; Wang, Y. R.; Fu, L. H.; Liu, Z. J.; Liu, S. T. 3D-motion phase modulation for protecting image information. *Appl. Phys. Lett.* **2023**, *123*, 021109.

[11] Wang, Z.; Sebek, M.; Liang, X. A.; Elbanna, A.; Nemati, A.; Zhang, N.; Goh, C. H. K.; Jiang, M. T.; Pan, J. S.; Shen, Z. X. et al. Greatly enhanced resonant exciton-trion conversion in electrically modulated atomically thin WS_2 at room temperature. *Adv. Mater.* **2023**, *35*, 2302248.

[12] Zhang, Q. Y.; Sun, H.; Tang, J. C.; Dai, X. C.; Wang, Z.; Ning, C. Z. Prolonging valley polarization lifetime through gate-controlled exciton-to-trion conversion in monolayer molybdenum ditelluride. *Nat. Commun.* **2022**, *13*, 4101.

[13] Das, S.; Huang, D.; Verzhbitskiy, I. A.; Ooi, Z. E.; Lau, C. S.; Lee, R.; Wong, C. P. Y.; Goh, K. E. J. Electrical control of valley polarized

charged exciton species in monolayer WS_2. *ACS Nano* **2024**, *18*, 30805–30815.

[14] Wang, Y. H.; Nie, Z. H.; Wang, F. Q. Modulation of photocarrier relaxation dynamics in two-dimensional semiconductors. *Light Sci. Appl.* **2020**, *9*, 192.

[15] Lin, K. Q.; Ziegler, J. D.; Semina, M. A.; Mamedov, J. V.; Watanabe, K.; Taniguchi, T.; Bange, S.; Chernikov, A.; Glazov, M. M.; Lupton, J. M. High-lying valley-polarized trions in 2D semiconductors. *Nat. Commun.* **2022**, *13*, 6980.

[16] Lee, H.; Koo, Y.; Choi, J.; Kumar, S.; Lee, H. T.; Ji, G.; Choi, S. H.; Kang, M.; Kim, K. K.; Park, H. R. et al. Drift-dominant exciton funneling and trion conversion in 2D semiconductors on the nanogap. *Sci. Adv.,* **2022**, *8*, eabm5236.

[17] Zhang, F.; Guo, Y. H.; Pu, M. B.; Chen, L. W.; Xu, M. F.; Liao, M. H.; Li, L. T.; Li, X.; Ma, X. L.; Luo, X. G. Meta-optics empowered vector visual cryptography for high security and rapid decryption. *Nat. Commun.* **2023**, *14*, 1946.

[18] Liu, L.; Zhang, X. T.; Zhang, Q.; Zhang, M. W.; Zhang, X. T.; Zhang, P. H.; Zhao, C. Y.; Gan, X. T. Reconfigurable logic of multidimensional encryption based on $ReSe_2$ homojunction photodetector. *ACS Nano* **2025**, *19*, 25490–25500.

[19] Ram, A.; Maity, K.; Marchand, C.; Mahmoudi, A.; Kshirsagar, A. R.; Soliman, M.; Taniguchi, T.; Watanabe, K.; Doudin, B.; Ouerghi, A. et al. Reconfigurable multifunctional van der waals ferroelectric devices and logic circuits. *ACS Nano* **2023**, *17*, 21865–21877.

[20] Huang, J. N.; Hoang, T. B.; Mikkelsen, M. H. Probing the origin of excitonic states in monolayer WSe_2. *Sci. Rep.* **2016**, *6*, 22414.

[21] Cho, C.; Wong, J.; Taqieddin, A.; Biswas, S.; Aluru, N. R.; Nam, S.; Atwater, H. A. Highly strain-tunable interlayer excitons in MoS_2/WSe_2 heterobilayers. *Nano Lett.* **2021**, *21*, 3956–3964.

[22] Sun, X. Z.; Chen, Y.; Li, Z. W.; Han, Y.; Zhou, Q.; Wang, B. B.; Taniguchi, T.; Watanabe, K.; Zhao, A. D.; Wang, J. L. et al. Visualizing band profiles of gate-tunable junctions in MoS_2/WSe_2 heterostructure transistors. *ACS Nano* **2021**, *15*, 16314–16321.

[23] Xiao, K.; Yan, T. F.; Xiao, C. X.; Fan, F. R.; Duan, R. H.; Liu, Z.; Watanabe, K.; Taniguchi, T.; Parkin, S. S. P.; Yao, W. et al. Exciton-exciton interaction in monolayer $MoSe_2$ from mutual screening of coulomb binding. *ACS Nano* **2024**, *18*, 31869–31876.

[24] Cunningham, P. D.; Hanbicki, A. T.; McCreary, K. M.; Jonker, B. T. Photoinduced bandgap renormalization and exciton binding energy reduction in WS_2. *ACS Nano* **2017**, *11*, 12601–12608.

[25] Ugeda, M. M.; Bradley, A. J.; Shi, S. F.; da Jornada, F. H.; Zhang, Y.; Qiu, D. Y.; Ruan, W.; Mo, S. K.; Hussain, Z.; Shen, Z. X. et al. Giant bandgap renormalization and excitonic effects in a monolayer transition metal dichalcogenide semiconductor. *Nat. Mater.* **2014**, *13*, 1091–1095.

[26] Cong, X.; Mohammadi, P. A.; Zheng, M. Y.; Watanabe, K.; Taniguchi, T.; Rhodes, D.; Zhang, X. X. Interplay of valley polarized dark trion and dark exciton-polaron in monolayer WSe_2. *Nat. Commun.* **2023**, *14*, 5657.

[27] Massicotte, M.; Vialla, F.; Schmidt, P.; Lundeberg, M. B.; Latini, S.; Haastrup, S.; Danovich, M.; Davydovskaya, D.; Watanabe, K.; Taniguchi, T. et al. Dissociation of two-dimensional excitons in monolayer WSe_2. *Nat. Commun.* **2018**, *9*, 1633.

[28] Zhu, B. R.; Xiao, K.; Yang, S. Y.; Watanabe, K.; Taniguchi, T.; Cui, X. D. In-plane electric-field-induced orbital hybridization of excitonic states in monolayer WSe_2. *Phys. Rev. Lett.* **2023**, *131*, 036901.

[29] Waheed, Y.; Shit, S.; Surendran, J. T.; Prasad, I. D.; Watanabe, K.; Taniguchi, T.; Kumar, S. Large trion binding energy in monolayer WS_2 via strain-enhanced electron-phonon coupling. *Commun. Mater.* **2025**, *6*, 86.

[30] Zhumagulov, Y. V.; Perebeinos, V. Perspective on trions and excitons in two-dimensional atomically thin materials. *Appl. Phys. Lett.* **2024**, *125*, 250501.

[31] Dery, H.; Robert, C.; Crooker, S. A.; Marie, X.; Van Tuan, D. Energy shifts and broadening of excitonic resonances in electrostatically doped semiconductors. *Phys. Rev. X* **2025**, *15*, 031049.